Positronium emission from MgO smoke nanocrystals

View the article online for updates and enhancements.

IOP ebooks™

Bringing you innovative digital publishing with leading voices to create your essential collection of books in STEM research.

Start exploring the collection - download the first chapter of every title for free.

IOP Publishing

Positronium emission from MgO smoke nanocrystals

L Gurung[1], A M Alonso[1], T J Babij[2], B S Cooper[1], A L Shluger[1,3] and **D B Cassidy[1]**

[1] Department of Physics and Astronomy, University College London, Gower Street, London, WC1E 6BT, United Kingdom
[2] Plasma Research Laboratory, Research School of Physics and Engineering, Australian National University, Canberra ACT 2601, Australia
[3] London Centre for Nanotechnology, University College London, Gower Street, London, WC1E 6BT, United Kingdom

E-mail: d.cassidy@ucl.ac.uk

CrossMark

Abstract

We report experiments in which positronium (Ps) atoms were created in a thick layer of MgO smoke powder deposited on a thin silicon nitride substrate. The experimental arrangement was such that a positron beam could be implanted directly into the top of the MgO layer or be transmitted through the substrate, allowing Ps to be produced within $\approx$100 nm or 30 μm of the powder-vacuum interface. The transverse kinetic energy of Ps atoms emitted into vacuum was measured via the Doppler broadening of $1^3S_1 \rightarrow 2^3P_J$ transitions, and found to be $E_x \approx 350$ meV, regardless of how far Ps atoms had traveled through the powder layer. Our data are not consistent with the model in which energetic Ps atoms emitted into the internal free volume of a porous material are cooled via multiple surface collisions, and instead indicate that in nanocrystals lower energy Ps is generated, with negligible subsequent cooling in the large open volumes of the powder. Our experiments also demonstrate that SiN substrates coated with MgO smoke can provide a simple and inexpensive method for producing Ps transmission targets.

Keywords: positronium, MgO, tranmission

(Some figures may appear in colour only in the online journal)

1. Introduction

In 1968 Paulin and Ambrosino discovered that long-lived Positronium (Ps) [1] atoms are produced in fine granulated powders of SiO_2, Al_2O_3, and MgO following irradiation with energetic positrons [2]. Using positron annihilation lifetime spectroscopy (PALS) they measured a long-lived Ps lifetime component that was comparable to the 142 ns vacuum lifetime [3], and whose intensity was dependent on the specific surface area of the sample. These observations were explained by Brandt and Paulin [4], who suggested that slow positrons could form Ps atoms in the bulk insulator material which could then diffuse to the grain surfaces and be emitted into the inter-granular spaces and decay at a rate similar to the vacuum rate.

Since then Ps formation in many oxides (and other insulating materials) has been observed [5] and it is now known that Ps formation in insulators may occur via surface or bulk processes, both of which will typically result in atoms emitted with $\approx$eV energies. Recent studies have indicated that in SiO_2 both surface and bulk Ps formation occurs [6], whereas in Al_2O_3 [7] and MgO [8] Ps formation is most likely generated only via surface processes.

The long lifetimes of energetic Ps generated in insulating powders (whether by bulk or surface mechanisms) imply that multiple interactions with the internal surfaces do not necessarily lead to significant annihilation losses. Such interactions

J. Phys. B: At. Mol. Opt. Phys. **52** (2019) 105004

L Gurung *et al*

may, however, result in Ps cooling, as demonstrated by Chang and co-workers in silica aerogel [9]. Thus, the energy with which Ps is ultimately emitted into vacuum from porous insulating materials may be considerably lower than the initial Ps formation energy. The kinetic energy of Ps atoms emitted directly into vacuum from single crystal surfaces of MgO and SiO_2 has been measured by time-of-flight (TOF) spectroscopy and found to be ≈ 4 and 3 eV, respectively [10]. In other measurements a 1 eV component from SiO_2 has also been seen, with the 1 and 3 eV components attributed to bulk and surface formation respectively [6]. However, the kinetic energy of Ps emitted from MgO smoke powder measured by Curry and Schawlow [11], also using TOF spectroscopy, was found to be 0.28 ± 0.1 eV. Similarly, TOF measurements by Mills and co-workers revealed 0.19 eV Ps emitted from a thick layer of room temperature SiO_2 powder [12]. These observations appear to support the model of energetic Ps cooling down via interactions within porous structures [4] insofar as they exhibit sub-eV Ps emission.

Here we present measurements of the kinetic energy of Ps emitted into vacuum from MgO smoke powder. Ps was generated near the top of the layer, by low-energy implantation, and from the back of the powder after implanting positrons through a thin (50 nm) Si_3N_4 (henceforth SiN) substrate. In the former case Ps atoms were emitted from a mean depth of ≈ 100 nm. In the latter case the positrons penetrate only a few microns into the MgO, and Ps atoms must therefore travel through most of the $\approx 30\,\mu$m thick layer to reach vacuum. The kinetic energy of Ps emitted into vacuum from both configurations was measured via Doppler broadening spectroscopy, and a constant (transverse) Ps energy of ≈ 350 meV was observed. Our data are inconsistent with the emission and subsequent cooling of ≈ 4 eV Ps, and instead indicate that lower energy Ps is emitted from MgO nanocrystals, and that it experiences negligible cooling in the large internal voids.

2. Experimental methods

2.1. Ps excitation and detection

The experimental apparatus and measurement techniques used in this work are described in detail elsewhere [13, 14]. A two-stage Surko type buffer gas trap [15] was used to generate a pulsed positron beam containing $\approx 10^5$ positrons in a 3 ns, 4 mm spot (FWHM) at 1 Hz. The beam was implanted into a SiN–MgO target, and the resulting Ps atoms were probed by two simultaneously applied pulsed lasers. These were Nd:YAG pumped dye lasers with ultra-violet (UV) light at $\lambda = 243$ nm and infra-red (IR) light at $\lambda = 729$–760 nm. The UV laser was used to drive $1^3S_1 \rightarrow 2^3P_J$ transitions, and the IR laser was used either to photoionize $n = 2$ atoms or to excite them to long-lived Rydberg levels via $2^3P_J \rightarrow n^3D_J/n^3S_J$ transitions. Here the positron beam direction was along the z axis, the target was in the x–y plane, and the laser propagation was along the x direction.
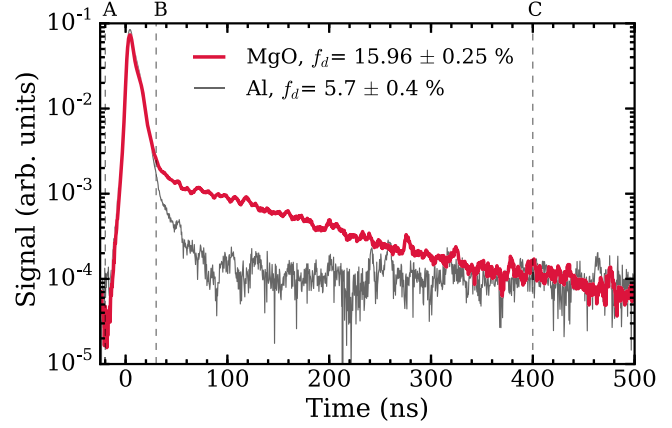
Figure 1. Lifetime spectra recorded by a PWO detector for 3 keV positrons implanted into a layer of MgO and an untreated Al plate. The dashed vertical lines indicate the analysis time windows used to obtain f_d, as explained in the text.

The production of Ps atoms was monitored using a single-shot version of PALS (SSPALS) [16] that involves the detection of pulsed Ps annihilation radiation in real time using fast detectors. In this work we use both lead tungstate (PWO) [17] and a lutetium yttrium oxyorthosilicate (LYSO) scintillators [18] coupled to photomultiplier tubes. These detectors have different light output and timing properties, making them useful in different scenarios. An example of Ps formation measured with a PWO detector is shown in figure 1. Here 3 keV positrons were implanted into a layer of MgO, and into an untreated Al plate. We expect that MgO will generate some Ps but that almost none will be produced by the Al plate. The amount of Ps present can be quantified by the parameter f_d which is is proportional to the amount of o-Ps present and is defined as

$$f_d = \int_B^C V(t)dt / \int_A^C V(t)dt, \qquad (1)$$

where $V(t)$ is the detector output voltage. The time windows used to analyze lifetime spectra (A, B, C) depend on the detectors used and the type of event being studied. Typically for photoionization events we use $(-20, 30, 400)$ and $(-20, 70, 600)$ ns for PWO and LYSO respectively. We take the lifetime spectra produced from Al to be the background, and obtain a $f_{bk} = 5.7\% \pm 0.4\%$. As a crude approximation the actual fraction of implanted positrons that form long-lived Ps atoms may be estimated to be $F_{Ps} = 2 \times [f_d - f_{bk}]$ [19].

The interaction of the laser light with Ps atoms can change the amount of long-lived Ps present, either by forcing atoms to annihilate, or by promoting them to longer-lived states. Laser-induced changes in f_d are quantified by the parameter S_γ defined as

$$S_\gamma = \frac{f_{d(off)} - f_{d(on)}}{f_{d(off)}}, \qquad (2)$$

where $f_{d(on)}$ and $f_{d(off)}$ refer to measurements made with the excitation lasers on and off resonance [13].

The SiN–MgO target was mounted so that it could be rotated by 180°, allowing either side to face the incident

J. Phys. B: At. Mol. Opt. Phys. **52** (2019) 105004

L Gurung *et al*
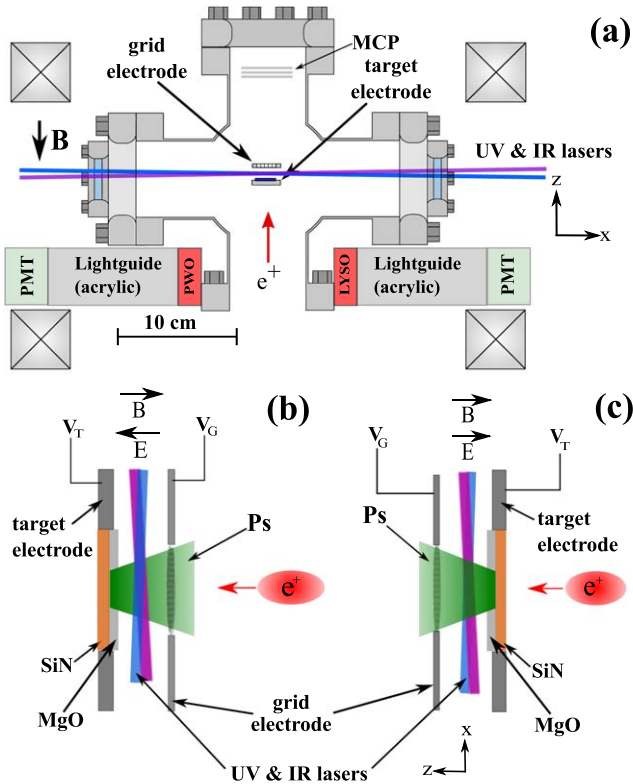
Figure 2. A schematic of the target chamber, laser beam, and detector positions (a), and the target orientation with respect to the incident positron beams for reflection (b) and transmission (c) operation. The grid electrode was situated 10 mm in front of the target electrode and contained a 90% transmission mesh.

positron beam, as indicated in figure 2. A grid electrode was mounted in front of the MgO side and used to control the electric field during laser excitation of Ps. The beam implantation energy E_B was controlled by the voltage applied to the grid/target electrodes.

2.2. Target preparation

To make the target a 10 cm long strip of magnesium ribbon weighing ∼0.15 g was combusted in air, and the resulting oxide smoke was collected on the front surface of a SiN membrane held ∼10 cm above the flame. The manufacturer (Norcada) specified SiN dimensions were 5 mm × 5 mm × 50 nm, and the film was mounted on a 200 μm thick silicon frame. Within 30 min of fabrication the target was mounted on an electrode structure and inserted into the experimental chamber, which was then pumped out to a pressure below 10^{-9} mbar.

To estimate the thickness of the MgO layer the same combustion-deposition procedure as described above was performed, using thin (0.1 mm) Cu foil with an area of 4 cm². The foil was weighed before and after MgO deposition, and the powder weight found to be 3.9 ± 0.1 mg. Assuming a powder density [2] of 0.35 g cm^{-3} we find a layer thickness on the order of 30 μm. As we have no independent verification of the powder density in our experiments this must be considered as an approximation.
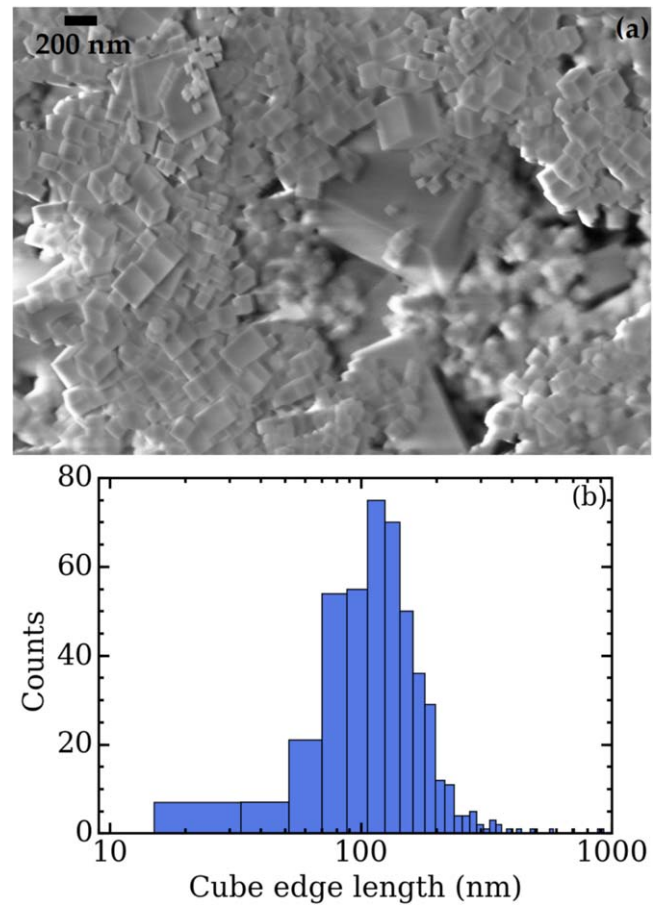
Figure 3. (a) A Karl Zeiss XB1540 scanning electron microscope (SEM) image of MgO smoke nanocrystals deposited on a Cu plate obtained with an electron beam energy of 3 keV. (b) MgO cube edge length distribution obtained from the SEM image in (a) using particle size analysis software ImageJ [25].

A scanning electron microscope (SEM) image of MgO smoke collected on a 1 mm thick Cu plate is shown in figure 3(a); it reveals cubic structures of MgO with varying crystal edge lengths. The formation of MgO(100) single-crystal cubes after burning Mg in air is a well-known phenomena that has been widely studied [20–22]. Similarly, ion implantation and annealing in MgO single crystals can result in the formation of stable internal rectangular nano-voids [8, 23]. The distribution of crystal sizes obtained from Mg combustion in air depends to some degree on various synthesis conditions, including humidity, Mg purity, flame temperature, and oxygen partial pressure [24]. In general, however, highly asymmetric distributions are observed, with cube sizes ranging from a few nm to several microns. Our SEM images were analyzed using particle size analysis software, ImageJ [25], and the results are shown in figure 3(b). We find a broad cube size distribution, ranging from 10 nm to 1 μm, with a mean cube edge length of ≈140 nm, and correspondingly distributed open volumes between the single crystal cubes. The MgO thickness and cube size distributions are not expected to be significantly different using SiN substrates.

J. Phys. B: At. Mol. Opt. Phys. **52** (2019) 105004

L Gurung *et al*

2.3. Positron energy loss and stopping profiles

The transmission of positrons through the SiN substrate can be described using standard positron stopping profiles. These have been widely studied in the context of positron annihilation based depth profiling which is used, for example, to characterize multi-layer thin films [26]. Good agreement is found between disparate materials, including metals [27] and amorphous polymers [28], suggesting that positron implantation profiles are largely independent of structure and depend only on the mass density for typical experimental conditions. Because of this, positron stopping profiles in a wide range of materials are frequently approximated by the Makhovian stopping profile $P(z)$, which may be expressed as [29]

$$P(z) = \frac{mz^{m-1}}{z_0^m} \exp\{\{-(z/z_0)^m\}\}, \qquad (3)$$

where $z_0 = \bar{z}/\Gamma(1 + (1/m))$, m is a material dependent (shape) parameter. $\bar{z}$ is defined as the mean implantation depth of positrons with energy K (units of keV) into a material of density ρ (g cm^{-3}) given by [27]

$$\bar{z} = \frac{AK^\nu}{\rho}, \qquad (4)$$

where the values of A, ν and m depend on the material. The implantation of positrons into the MgO powder can also be approximated using the same Mahkov description. However, the accuracy will depend on how well the mean density is known, and the model will be less applicable for low implantation energies owing to the structure of the powder. The true density of MgO is ≈ 3.5 gcm^{-3} but for powder it is approximately an order of magnitude lower [2]. Estimated positron implantation profiles in MgO powder are shown in figure 4(a). The lowest energy direct implantation depth is ≈ 100nm. The implantation profiles obtained using equations (3) and (4), with the parameters $A = 3.3\,\mu$g cm^{-2}, $\nu = 1.7$, $m = 2$, $\rho \sim 3$ g cm^{-3} for SiN [30] are shown in figure 4(b). Also indicated in the figure is the fraction of each distribution that would be transmitted through the SiN substrate into the MgO layer.

Figure 4(c) shows the positron energy loss, and approximate subsequent penetration into the MgO layer as a function of the incident positron energy. The energy loss data were obtained from the NIST stopping power and range tables for electrons (ESTAR) database [31]. Note that no data is available below 1 keV. These data were generated using the Bethe–Bloch equation, with an interpolated database of shell and density corrections. They are expected to be accurate to less than 10% for energies below 10 keV, at which level of precision electron and positron stopping profiles are effectively the same.

Figure 4 indicates that in the transmission configuration a positron beam energy $\geqslant 2$ keV is needed for a significant fraction of the beam to traverse the SiN substrate, and that even at 6 keV the positrons would not penetrate more than $\approx 1\,\mu$m into the MgO. Therefore all Ps atoms produced in the transmission mode have to travel through $\approx 30\,\mu$m of MgO powder to reach vacuum.
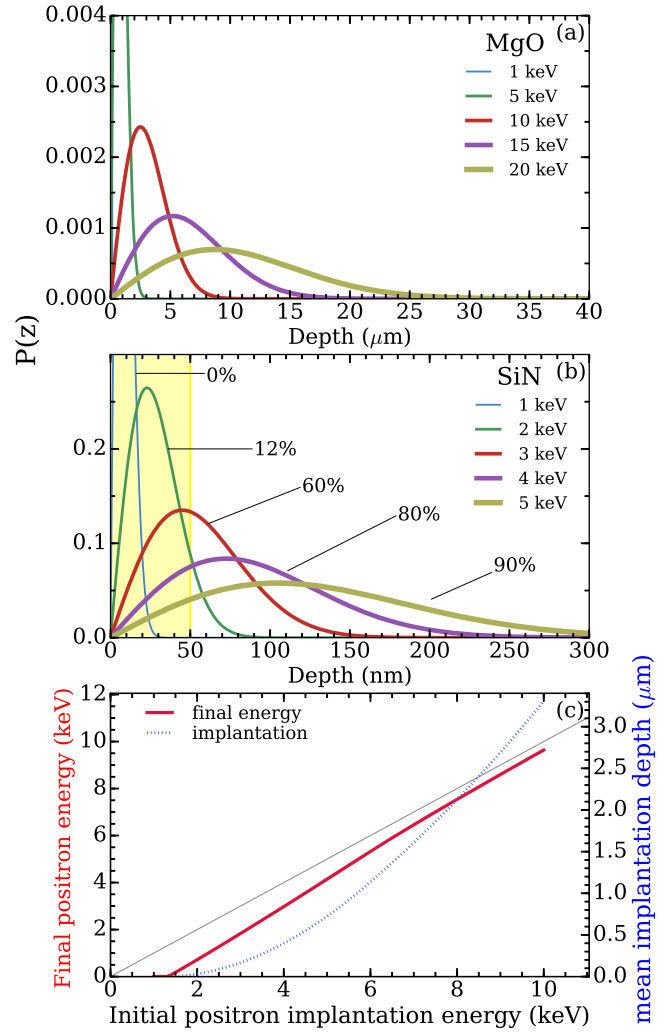

Figure 4. Positron implantation profiles for different energies in (a) MgO and (b) SiN calculated using equation (3). The yellow bar in (b) represents the 50 nm SiN film thickness. The approximate fraction of each distribution transmitted through the SiN is also indicated. The 1000 V profile has been truncated vertically for clarity. (c) Energy of transmitted positrons (solid red line) as a function of implantation energy by monoenergetic positrons in a 50 nm SiN film. The thin straight lines corresponds to no energy loss. The corresponding mean implantation depth into an MgO layer, assuming a powder density of 0.35 g cm^{-3} is also shown (dotted blue line).

3. Results and discussion

3.1. Positronium formation

The production of Ps atoms following positron implantation into the target in both reflection and transmission modes was measured via single shot lifetime spectroscopy, as described in section 2.1. The background subtracted values of f_d are shown in figure 5(a). When positrons are directly implanted into the MgO (reflection mode), f_d decreases with increasing E_B. A similar effect is observed in mesoporous silica, and is attributed to Ps annihilation losses following surface interactions as the atoms leave the pore network. This idea is supported by the concomitant Ps cooling [32]. This model does not explain the reduction in f_d observed in MgO because
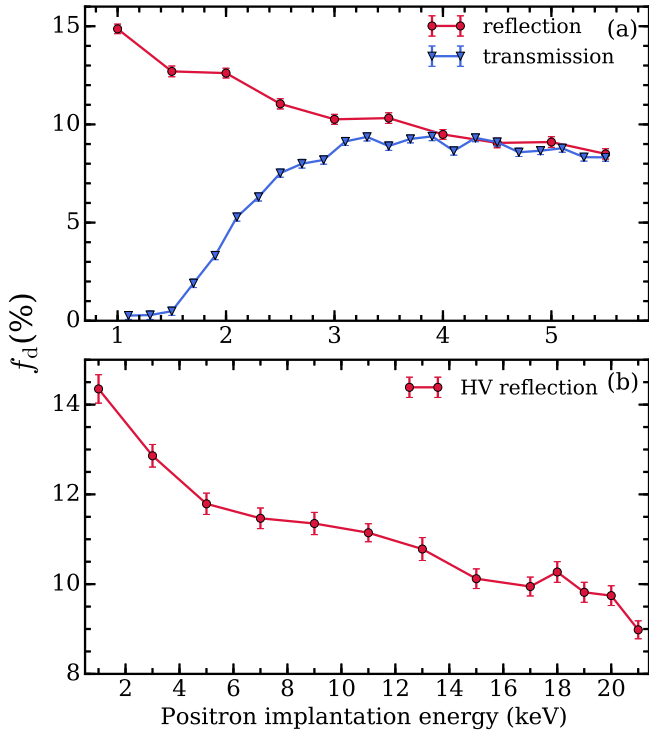
Figure 5. (a) Background subtracted f_d measurements recorded using a PWO detector as a function of positron energy in reflection (circles) and transmission (triangles) orientations (see figure 2) and (b) high voltage test measurements designed to estimate the MgO thickness, as described in the text.

there is no associated cooling. The open volumes in MgO powder are much larger than the voids in mesoporous silica, and the scattering rate is therefore much lower, which prevents both Ps thermalization and annihilation. MgO powder also differs from mesoporous silica in that it has a very broad distribution of crystal sizes. Therefore, at higher beam energies it is possible for positrons to be implanted deeper into larger crystals, reducing the probability of diffusion to the crystal surface.

The positron diffusion length in MgO is 14 ± 1 nm [33], meaning that positrons implanted much deeper than this into individual large crystals will not form Ps. By comparison, in mesoporous SiO_2 films [34] Ps is primarily formed in the bulk material, and the Ps diffusion length (11 ± 1) nm [33] is generally larger than distance to an internal surface. Hence, the *formation* of Ps in such films is largely independent of the beam energy [35], but the subsequent transmission of Ps into vacuum is not. Conversely, in MgO smoke Ps formation is inhibited at higher beam energies, while Ps transmission through the voids is unaffected.

The almost monotonic decrease in f_d observed in figure 5(a) for reflection mode indicates that positrons are not penetrating the MgO layer and stopping in the SiN substrate. When positrons are implanted into the SiN side of the target (transmission mode), f_d increases with increasing beam energy from zero up to a level commensurate with the reflection mode measurement. This occurs because at higher implantation energies positrons start to penetrate the SiN, enter the MgO layer and form Ps. The dependence of the

increase in f_d with the Ps beam energy is consistent with the expected positron transmission fractions shown in figure 4(b). For those positrons that do penetrate the SiN, the fraction of energy lost is relatively small, as indicated in figure 4(c), and therefore the penetration into the MgO crystals (and hence Ps formation efficiency) is very similar to that observed in reflection mode.

The rotating sample arrangement (see figure 2) was designed to withstand voltages $\leqslant 6$ kV. In order to check the MgO layer thickness a test measurement was performed using an apparatus in which much higher voltages could be applied to the target. These data are shown in figure 5(b). Here an isolated copper foil with MgO prepared in the standard way was bombarded with positrons with energies up to 21 keV. If a significant fraction of the positron beam were to penetrate the MgO layer and enter the Cu substrate we would expect to see a sudden decrease in f_d. No such decline in Ps production was observed even at 21 keV, which is consistent with an MgO layer larger than $\approx 20 \, \mu$m (see figure 4(a)). These data are therefore consistent with the $\approx 30 \, \mu$m estimate described in section 2.2.

3.2. Positronium energy

The mean transverse kinetic energy of Ps atoms emitted into vacuum was measured using Doppler broadening spectroscopy [32]. UV and IR light traveling parallel to the target surface (as shown in figure 2) was used to drive $1^3S_1 \rightarrow 2^3P_J$ transitions, and to photoionize the 2^3P_J atoms. Positrons liberated via photoionization were accelerated back into the target due to the applied electric field, leading to annihilation. This process changes f_d, and thus also S_γ (see equation (2)). The width of the $1^3S_1 \rightarrow 2^3P_J$ transition is dominated by Doppler broadening, and can therefore be used to infer the Ps velocity spread in the direction of the UV laser. Line shapes measured for Ps produced in reflection and transmission modes are shown in figure 6 for different positron beam energies. These data are fitted to

$$S(\lambda) = A \exp \frac{-(\lambda - \lambda_0)^2}{2\sigma^2}, \quad (5)$$

where σ and λ_0 are the Gaussian width and the resonance wavelength respectively. The mean squared Ps velocity in the direction of laser propagation is $\langle v_x^2 \rangle = [c\sigma/\lambda_0]^2$, and the kinetic energy $E_x = E_y = \frac{1}{2}m_{Ps}v_x^2$. Here we assume that the x and y components are the same. The energies derived in this way from the data in figure 6 are shown in figure 7. The measured Ps energies showed no dependence on the positron beam energy, or even whether the Ps was produced in the refection or transmission configuration. Although there is some statistical variation, all measured energies are consistent with each other. For the reflection and transmission modes the mean Ps energies obtained from the Doppler profiles were $E_x = 340 \pm 143$ meV, and $E_x = 337 \pm 115$ meV, respectively.

Ps emission from the MgO surfaces is expected to be essentially isotropic owing to the random distribution of nanocrystals, although Ps that is emitted into vacuum may
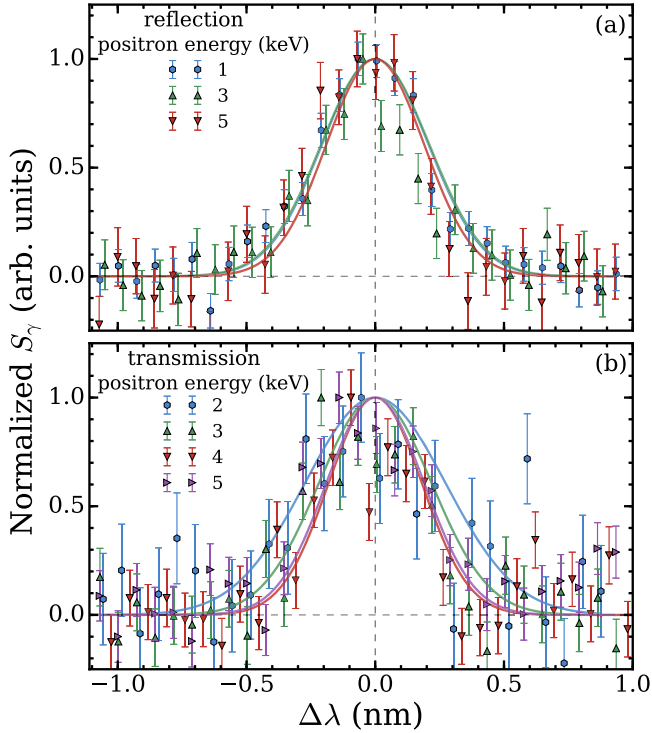
Figure 6. $1\,^3S_1 \rightarrow 2\,^3P_J$ transition line shapes for Ps excited in a reflection geometry (a) and a transmission geometry (b) at various positron beam energies plotted as a function of detuned wavelength. The line shapes are centered around ~243 nm and the solid lines are Gaussian fits using equation (5). These data were recorded using a LYSO detector.
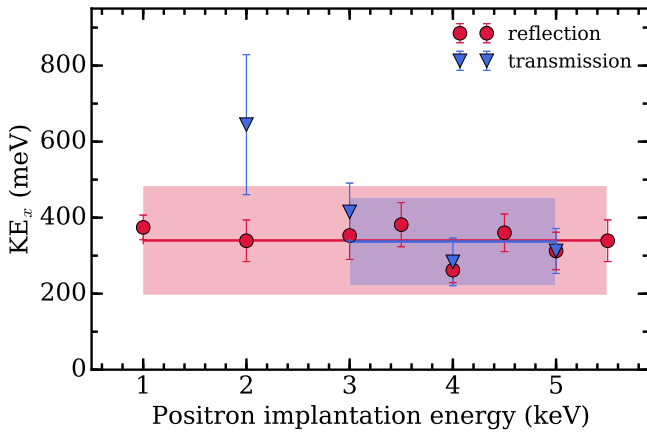
Figure 7. Transverse kinetic energy of Ps atoms produced in reflection (red circles) and transmission (blue triangles) modes for different positron beam energies. The solid lines indicate the mean of the measurements and the shaded bars the standard deviation. The 2 keV transmission data point has not been included in the average value owing to the low Ps signal at this energy (see figure 5(a)).

tend to be slightly forward directed. By simulating isotropic emission profiles for the Doppler data shown in figure 6 we find that the observed Gaussian-like profiles can only be obtained if the Ps has an intrinsic energy spread on the order of the standard error (i.e. ≈100 meV). Similarly, we can also rule out the presence of an additional Ps component with energies ⩾1 eV with intensities more than 30% of the low-
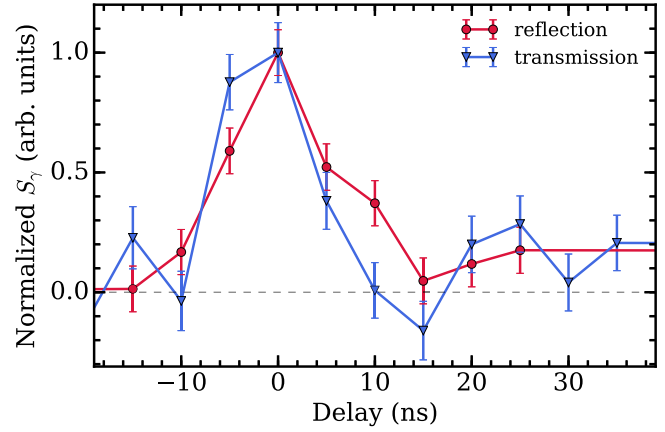

Figure 8. Laser pulse delay relative to positron implantation measured in the reflection and transmission configurations, with positron beam energies of 1 and 4 keV, respectively.

energy component. This was done by adding a fast component to the Doppler profiles and estimating the extent to which this component affects the quality of the (single component) Gaussian fits.

Beam-based TOF measurements were conducted by Sferlazzo, Berko, and Canter using single-crystal MgO(100) surfaces [10]. They observed Ps emission with a broad energy distribution, peaking at around 4 eV with a tail extending up to more than 10 eV. A lower peak energy of 2.6 eV was measured by Nagashima and co-workers [6], who also observed a broad energy spread. The small MgO(100) nanocrystals in a powder sample might be expected to emit Ps with a similar distribution of energies. However, this is not consistent with our data, since the Ps generated at low beam energies in the reflection mode would experience only minimal cooling, and should therefore be emitted with almost the original energy distribution. The fact that the observed energies are essentially constant for *all* implantation energies and configurations implies that Ps cooling in MgO smoke powder is negligible.

If significant energy loss were taking place we would expect that the amount of time taken for Ps atoms to be emitted into vacuum would be different between reflection and transmission measurements [36]. A relative measurement of the Ps emission time can be obtained from the laser-delays needed to optimize the excitation signals. The laser-target alignment procedure places the laser beam approximately 1 mm in front of the target surface. Scanning the laser delay to optimize the temporal overlap with the Ps atoms as they leave the target will then reveal any difference in the Ps emission time, limited by the reproducibility of the beam aliment and the temporal width of the laser pulse (≈5 ns). Figure 8 shows such scans, measured in the transmission and reflection configurations. These data show that the Ps emission time is almost the same in both configurations, which is consistent with a low cooling rate. This suggests that long open channels are formed in the powder samples, allowing Ps atoms to travel with mean free paths on the order of a micron, and with relatively few collisions.

J. Phys. B: At. Mol. Opt. Phys. **52** (2019) 105004

L Gurung *et al*
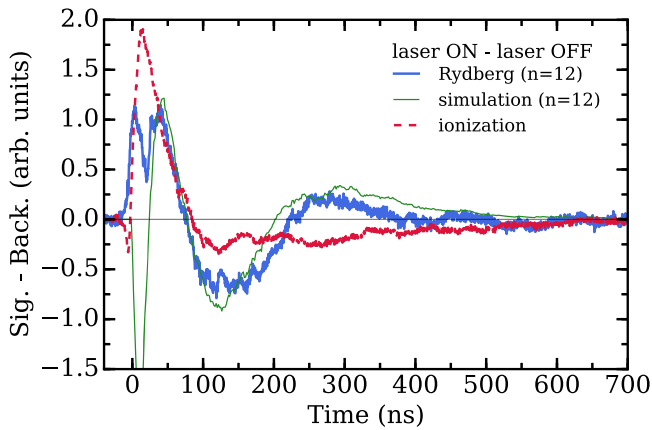
Figure 9. Laser-induced changes in the time profile of Ps annihilation radiation, recorded following the excitation of the $n = 12$ Rydberg Ps atoms in the transmission mode (thick blue line). Also shown is the same measurement with the IR laser tuned to photoionize Ps (red dashed line) and a Monte–Carlo simulation of the Ps production and decay (thin green line), as explained in the text.

The Doppler profiles shown in figure 6 provide a measure of the transverse Ps velocities. To estimate their longitudinal speeds, Ps atoms were excited to $n = 12$ Rydberg states that have radiative lifetimes of $\approx 5\,\mu s$ [37], allowing for TOF measurements over a much longer time scale than is possible for ground state atoms. Rydberg Ps atoms were produced by tuning the IR laser wavelength to 749.84 nm to drive $2^3P_J \rightarrow 12^3D/12^3S$ transitions. Rydberg Ps emitted in the transmission orientation was then able to travel towards the grid electrode ($\Delta z = 1$ cm) and then further upstream towards a microchannel plate (MCP) detector ($\Delta z = 8$ cm), as indicated in figure 2. Measurements of laser-induced changes in Ps annihilation rates are shown in figure 9. These data were obtained by subtracting spectra measured without laser excitation (Back) from spectra obtained with laser irradiation (Sig). This produces a difference curve that indicates changes in the amount of annihilation radiation present relative to the ground state decay [13]. Thus, a positive signal denotes excess annihilations, while a negative signal indicates fewer annihilation events. The data in figure 9 represent two cases, Rydberg production and photoionization.

The ionization data in figure 9 exhibit a peak at $t \approx 0$ (i.e. just after the Ps is produced) caused by the annihilation of positrons liberated following photoionization, with a subsequent reduction in decay events thereafter. The Rydberg data show positive peaks close to 40 and 300 ns caused by Ps collisions with the grid electrode and the MCP, respectively. By matching a Monte Carlo simulation of Ps trajectories (including the full vacuum chamber geometry) to the measured TOF data we obtained estimates for the Ps longitudinal speeds (that is, the mean Ps speed in the z direction, perpendicular to the target). These correspond to kinetic energies of $E_z \approx 425 \pm 50$ meV, which is consistent with the Doppler broadening measurements. The simulations employed a cosine Ps angular distribution as this was found to be broadly consistent with the measured data. The size and shape of the vacuum chamber meant the delayed Ps

annihilation profiles were sensitive to both the angular and velocity distributions, whereas the early profiles (caused by collisions with the nearby grid electrode, see figure 2) were mostly sensitive to the velocity distribution.

The total emission energies are not directly measured by Doppler broadening or by TOF spectroscopy. For a known angular distribution one could add the components measured in different directions to obtain the total emission energy. However, the orientation of the nanocrystal surfaces is unknown, and hence so is the Ps angular distribution. If we assume that the cosine approximation is valid then we can infer that the total Ps emission energies are on the order of 1 eV. We note that we can make a direct comparison between our single component data with other TOF measurements using powder samples (i.e. [11, 38]) as they will have similar angular distributions, and also measure only one component. The situation with single crystal samples is more complicated owing to their rough surfaces, which will give rise to different, but also unknown, angular emission profiles.

NB: the double peak observed at early times in the Rydberg data may be caused by ionization of some Rydberg atoms immediately after their creation by the excitation laser light, although signals of this type are subject to large fluctuations because of noise in the prompt peak and can also depend on how the spectra are normalized. This is not included in the simulation, and does not impact the TOF estimates obtained from the later peaks in these data.

Our measurements are consistent with those of Curry and Schawlow [11] who observed $E_z = 0.28 \pm 0.10$ eV Ps emission from a $\approx 6\,\mu m$ thick layer of MgO powder placed in front of a ^{22}Na source. This observation has been attributed to hot (several eV) Ps cooling in voids, but without an explicit measurement of the initial Ps energy such a process could not be confirmed. These data can also be explained by the formation of low-energy Ps atoms that experience minimal energy loss, just as we have measured.

This raises the question of why the emission of Ps atoms with energies E_z of several eV is observed from single crystal bulk MgO surfaces, while smoke nanocrystals appear to produce mostly low-energy Ps. In order to answer this it is necessary to consider the possible Ps formation processes in these materials. Two-dimensional angular correlation of annihilation (ACAR) studies of positrons in bulk MgO crystals do not show the narrow momentum components characteristic of bulk Ps [8, 10], suggesting that Ps formation in MgO is exclusively a surface process. As pointed out by Sferlazzo and co-workers [10], it is possible that Ps exists in bulk MgO in a weakly bound Mott–Wannier-like state [39], which would be susceptible to pick off decay and therefore would not necessarily be detectable via ACAR methods. These atoms are expected to be emitted with a broad distribution, with a maximum value approaching ≈ 5.8 eV, which could extend to higher values if Ps is not thermalized [10]. This mechanism is therefore not ruled out by previous observations of Ps emission from bulk crystals [6, 10].

It is also possible for Ps to be formed at MgO surfaces by positrons interacting with electrons excited into the conduction band by the incident positron beam. Energetic positrons

J. Phys. B: At. Mol. Opt. Phys. **52** (2019) 105004

L Gurung *et al*

implanted into MgO nanocrystals will thermalize by exciting electron-hole pairs. MgO has negative electron affinity, with the bottom of the conduction band at the surface located about 0.5–1.0 eV above the vacuum level [40, 41], meaning that a significant fraction of excited electrons will escape from the surface region. Some electrons, however, may become trapped in various surface states. It is known, for example, that in MgO nanocube powders, surface excitons can separate [42], and the resulting electrons may become trapped at Mg corner and kink sites [42, 43]. The energies of these electrons will depend on the surface site coordination, ranging from −0.6 eV (cube corner) to −2.0 eV (step kink) [43] below the vacuum level. The number of such sites depends on the physical geometry of the MgO; smoke nanocrystals are known to have flat surfaces [44], whereas bulk single crystal surfaces are generally very defective, even if polished [45, 46] or cleaved *in situ* [47, 48]. Thus, even though some electrons can be trapped at corner sites in nanocrystals, the number of electrons trapped at kink sites at surface steps on cleaved or polished MgO surfaces will be considerably higher. Ps formation resulting from the interaction with surface trapped electrons will be therefore much more likely at bulk surfaces.

For thermalized positrons with low momenta along the surface [49], the kinetic energy of emitted Ps is largely determined by the energy difference between the electron in MgO and in Ps, assuming Ps has zero or negative binding energy with the MgO surface. Electrons tunneling from localized corner and kink states can produce energetic Ps with a wide kinetic energy distribution peaking at about $K_{Ps} \approx E_{Ps} - E_e$, where $E_{Ps} = 6.8$ eV is the Ps binding energy in vacuum, and E_e is an average energy of electrons localized at low-coordinated surface sites at surfaces of MgO nanocrystals with respect to the vacuum level = 1.3 eV [43]. Ps produced in this way will have energies $K_{Ps} \approx 6.8 - 1.3 = 5.5$ eV. Therefore, this process is also not ruled out by previous observations of Ps emission from bulk crystals [6, 10]. In this case the precise surface conditions would dictate the angular emission profile but one would expect E_z to be several eV or more.

On the other hand, the top of the surface valence band of MgO bulk samples is about 6.7 ± 0.4 eV below the vacuum level [50–52]. If there are no available surface electrons, most of the Ps will be created by electrons tunneling from states in the valence band of MgO nanocrystals, which have energies E_e about 6.5 eV below the vacuum level and higher [43]. Therefore the kinetic energies of such Ps atoms are expected to peak at about $6.8 - 6.5 = 0.3$ eV, with a distribution due to the energy variations caused by different nanocrystal sizes. Again, the angular emission profiles would depend in this case on the nanocrystal orientations.

This mechanism is consistent with our observations. Our measurements do not rule out some fraction of energetic Ps formation, which we estimate to be less than 30%, as described above. Some amount of fast Ps may be expected owing to the presence of electrons trapped in corner and edge states. Surface electrons would be unlikely to affect Ps formed in the bulk, and our data therefore suggest that there is no weakly bound Mott–Wannier-like Ps in the bulk samples, and

that the Ps formation in those crystals occurs mainly via positron interactions with electrons trapped in surface states.

Our measured Ps energies are lower than those obtained by Gidley and co-workers [38], who measured a maximum Ps energy of $E_z = 0.8 \pm 0.2$ eV from MgO powder following the implantation of 400 eV positrons. These data exhibited a very broad distribution, with a significant component of slower Ps atoms having energies close to $E_z = 350$ meV (see figure 4 of [38]). The 400 eV beam energy used in this work is lower than we are able to apply in the present experiments because of the beam bunching method used [13], and it is possible that below some energy threshold the Ps formation mechanism in nanocrystals is more similar to the bulk crystal case. This may happen if spur electrons are closely associated with positrons in the near-surface region [53], giving rise to a larger fraction of energetic Ps (similar to that observed in bulk samples) as well as a low-energy component of the sort we have observed.

4. Conclusions

The data presented here show that Ps is emitted into vacuum from MgO smoke powder with essentially the same energy profile, regardless of the distance the atoms have to travel through the powder layer. This observation is inconsistent with the emission of atoms with several eV unless they are able to rapidly cool down to a few hundred meV, but cannot lose energy thereafter. The general picture of collisional cooling, which has been commonly accepted for many years [54], appears not to be correct in the case of MgO smoke nanocrystals. Our data suggest that in this case lower energy Ps is generated by thermal surface positrons interacting with valence electrons, and that there is very little cooling in the large open volumes of the powder. This Ps formation process is not the same as that observed in bulk MgO crystals, which have many more sites available for surface electron trapping.

Our experiments suggest that MgO smoke will not be useful for the generation of cold Ps atoms, although the procedure for coating thin SiN substrates does provide a simple and inexpensive method for producing Ps transmission targets [55–57]. These can be useful in experiments in which it is desirable to decouple positron beam transport and Ps production regions. For example, Ps scattering experiments [58], high-resolution TOF measurements [59] or precision spectroscopy of Ps [60].

It may be possible that the properties of MgO powder can be usefully applied to high-density Ps experiments [60, 61]. If an intense positron pulse is implanted into the right target it is possible to generate a spin-polarized Ps gas [62] which may form a Bose–Einstein condensate (BEC) if the temperature is low enough [63]. In order to achieve sufficiently high Ps densities the incident positron pulse must be so intense that it is likely to locally destroy the target [60]. If the positrons are implanted into a thick layer of MgO powder, however, then Ps atoms may be transported away from the energy deposition region and then be able to cool down and form a BEC.

J. Phys. B: At. Mol. Opt. Phys. **52** (2019) 105004

L Gurung *et al*

ORCID iDs

A L Shluger ![ORCID] https://orcid.org/0000-0002-2488-0896
D B Cassidy ![ORCID] https://orcid.org/0000-0001-8332-5553

References

[1] Wheeler J A 1946 *Ann. New York Acad. Sci.* **48** 219–38
[2] Paulin R and Ambrosino G 1968 *J. Phys. France* **29** 263–70
[3] Rich A 1981 *Rev. Mod. Phys.* **53** 127
[4] Brandt W and Paulin R 1968 *Phys. Rev. Lett.* **21** 193–5
[5] Sen P and Patro A P 1969 *Il Nuovo Cimento* B **64** 324–36
[6] Nagashima Y, Morinaka Y, Kurihara T, Nagai Y, Hyodo T, Shidara T and Nakahara K 1998 *Phys. Rev.* B **58** 12676–9
[7] Dauwe C and Mbungu-Tsumbu 1992 *Phys. Rev.* B **45** 9–19
[8] Eijt S, Falub C, van Veen A, Schut H, Mijnarends P, van Huis M and Fedorov A 2000 *MRS Proc.* **647** O14.11/R9.11
[9] Chang T, Xu M and Zeng X 1987 *Phys. Lett.* A **126** 189–94
[10] Sferlazzo P, Berko S and Canter K F 1987 *Phys. Rev.* B **35** 5315–8
[11] Curry S and Schawlow A 1971 *Phys. Lett.* A **37** 5–6
[12] Mills A P Jr, Shaw E D, Chichester R J and Zuckerman D M 1989 *Phys. Rev.* B **40** 2045–52
[13] Cooper B S, Alonso A M, Deller A, Wall T E and Cassidy D B 2015 *Rev. Sci. Instrum.* **86** 103101
[14] Alonso A M, Cooper B S, Deller A, Hogan S D and Cassidy D B 2016 *Phys. Rev.* A **93** 012506
[15] Danielson J R, Dubin D H E, Greaves R G and Surko C M 2015 *Rev. Mod. Phys.* **87** 247–306
[16] Cassidy D B, Deng S H M, Greaves R G and Mills A P Jr 2006 *Rev. Sci. Instrum.* **77** 073106
[17] Cassidy D B and Mills A P Jr 2007 *Nucl. Instrum. Meth.* A **580** 1338–43
[18] Alonso A M, Cooper B S, Deller A and Cassidy D B 2016 *Nucl. Instrum. Meth.* A **828** 163–9
[19] Cassidy D B, Hisakado T H, Tom H W K and Mills A P 2011 *Phys. Rev.* B **84** 195312
[20] Moodie A F and Warble C E 1971 *J. Cryst. Growth* **10** 26–38
[21] Coluccia S, Tench A J and Segall R L 1979 *J. Chem. Soc., Faraday Trans. 1* **75** 1769–79
[22] Jokes C F, Segall R L, Smart R S C and Turner P S 1980 *Philos. Mag.* A **42** 267–70
[23] Kooi B J, van Veen A, De Hosson J T M, Schut H, Fedorov A V and Labohm F 2000 *Appl. Phys. Lett.* **76** 1110–2
[24] Stankic S, Cottura M, Demaille D, Noguera C and Jupille J 2011 *J. Cryst. Growth* **329** 52–6
[25] Schneider C A, Rasband W S and Eliceiri K W 2012 *Nat. Methods* **9** 671
[26] Vehanen A, Saarinen K, Hautojärvi P and Huomo H 1987 *Phys. Rev.* B **35** 4606–10
[27] Mills A P Jr and Wilson R J 1982 *Phys. Rev.* A **26** 490–500
[28] Algers J, Sperr P, Egger W, Kögel G and Maurer F H J 2003 *Phys. Rev.* B **67** 125404
[29] Asoka Kumar P and Lynn K G 1990 *Appl. Phys. Lett.* **57** 1634–6
[30] O'Rourke B E, Zhou W, Oshima N, Ito K and Suzuki R 2013 *J. Phys.: Conf. Ser.* **443** 012069
[31] Berger M, Coursey J, Zucker M and Chang J Computer programs forcalculating stopping-power and range tables for electrons,protons, and helium ions (version 1.2.3) http://physics.nist.gov/Star
[32] Cassidy D B, Crivelli P, Hisakado T H, Liszkay L, Meligne V E, Perez P, Tom H W K and Mills A P Jr 2010 *Phys. Rev.* A **81** 012715
[33] Van Petegem S, Dauwe C, Van Hoecke T, De Baerdemaeker J and Segers D 2004 *Phys. Rev.* B **70** 115410
[34] Liszkay L *et al* 2008 *Appl. Phys. Lett.* **92** 063114
[35] Crivelli P, Gendotti U, Rubbia A, Liszkay L, Perez P and Corbel C 2010 *Phys. Rev.* A **81** 052703
[36] Cassidy D B, Hisakado T H, Meligne V E, Tom H W K and Mills A P Jr 2010 *Phys. Rev.* A **82** 052511
[37] Deller A, Alonso A M, Cooper B S, Hogan S D and Cassidy D B 2016 *Phys. Rev.* A **93** 062513
[38] Gidley D W, Zitzewitz P W, Marko K A and Rich A 1976 *Phys. Rev. Lett.* **37** 729–32
[39] Sato K, Shanai D, Hotani Y, Ougizawa T, Ito K, Hirata K and Kobayashi Y 2006 *Phys. Rev. Lett.* **96** 228302
[40] Rohlfing M, Wang N P, Krüger P and Pollmann J 2003 *Phys. Rev. Lett.* **91** 256802
[41] Baumeier B, Krüger P and Pollmann J 2007 *Phys. Rev.* B **76** 205404
[42] Sternig A, Stankic S, Müller M, Siedl N and Diwald O 2012 *Nanoscale* **4** 7494–500
[43] Sushko P V, Gavartin J L and Shluger A L 2002 *J. Phys. Chem.* C **106** 2269–76
[44] Scarano D, Bertarione S, Cesano F, Spoto G and Zecchina A 2004 *Surf. Sci.* **570** 155–66
[45] Crozier P A, Gajdardziska-Josifovska M and Cowley J M 1992 *Micros. Res. Tech.* **20** 426–38
[46] Benedetti S, Torelli P, Luches P, Gualtieri E, Rota A and Valeri S 2007 *Surf. Sci.* **601** 2636–40
[47] Barth C and Henry C R 2003 *Phys. Rev. Lett.* **91** 196102
[48] Barth C and Henry C R 2009 *J. Phys. Chem.* C **113** 247–53
[49] Levine R and Sander L 1982 *Solid State Commun.* **42** 5–8
[50] Ochs D, Maus-Friedrichs W, Brause M, Günster J, Kempter V, Puchin V, Shluger A and Kantorovich L 1996 *Surf. Sci.* **365** 557–71
[51] Kantorovich L N, Shluger A L, Sushko P V, Günster J, Stracke P, Goodman D W and Kempter V 1999 *Faraday Discuss.* **114** 173–94
[52] Sushko P V, Shluger A L and Catlow C A 2000 *Surf. Sci.* **450** 153–70
[53] Mogensen O E 1974 *J. Chem. Phys.* **60** 998–1004
[54] Ford G W, Sander L M and Witten T A 1976 *Phys. Rev. Lett.* **36** 1269–72
[55] Poulsen M R, Charlton M, Chevallier J, Deutch B I, Jorgensen L V and Laricchia G 1991 *J. Phys.: Condens. Matter.* **3** 2849
[56] Andersen S L, Johansen R R, Overgaard J B, Mortensen J K, Andersen K K, Thomsen H D, Lund M D, Chevallier J, Knudsen H and Uggerhøj U I 2014 *Eur. Phys. J.* D **68** 124
[57] Andersen S L, Cassidy D B, Chevallier J, Cooper B S, Deller A, Wall T E and Uggerhøj U I 2015 *J. Phys. B: At. Mol. Opt. Phys.* **48** 204003
[58] Swann A R, Cassidy D B, Deller A and Gribakin G F 2016 *Phys. Rev.* A **93** 052712
[59] Jones A C L, Rutbeck-Goldman H J, Hisakado T H, Piñeiro A M, Tom H W K, Mills A P Jr, Barbiellini B and Kuriplach J 2016 *Phys. Rev. Lett.* **117** 216402

J. Phys. B: At. Mol. Opt. Phys. **52** (2019) 105004

L Gurung *et al*

[60] Cassidy D B 2018 *Eur. Phys. J.* D **72** 53
[61] Mills A P Jr 2010 Physics with many positrons *Proc. of the International School of Physics 'Enrico Fermi'* 174 ed A Dupasquier, A P Mills Jr and R S Brusa pp 77–187
[62] Cassidy D B, Meligne V E and Mills A P Jr 2010 *Phys. Rev. Lett.* **104** 173401
[63] Platzman P M and Mills A P Jr 1994 *Phys. Rev.* B **49** 454–8